scientific reports

Check for updates

OPEN

A curvature-adaptive flexible capacitive sensing system for early detection of corrosion under insulation in long-distance thermal pipelines

Tao Zeng[1]✉, Songzhe Chai[1], Jinxin Xu[2] & Suan Xu[1]

Corrosion under insulation (CUI) poses a significant threat to the integrity and safety of long-distance thermal pipelines. However, conventional non-destructive testing (NDT) methods struggle to achieve early-stage detection of CUI while effectively balancing detection reliability, operational safety, and low cost. This paper presents a novel curvature-adaptive flexible array capacitive sensing system for the early identification of insulation defects, a critical precursor to CUI. The proposed system features a flexible capacitive probe with coplanar array electrodes on an adjustable substrate, allowing it to conform to various pipeline curvatures to enhance signal-to-noise ratio. A key innovation lies in the proposal of a novel approach for determining the depth of internal defects in thermal insulated pipelines, which leverages the stratified electric field generated by the electrode array and realizes defect depth estimation by analyzing the relative capacitance deviations across different electrode pairs. Furthermore, a feature decoupling method based on optimizing the sensor's lift-off height is introduced to distinguish between internal insulation defects and external protective jacket topography. To automate the process, an enhanced one-dimensional convolutional neural network is developed, achieving high-precision automated classification of jacket surface defects. Experimental results demonstrate the system's capability to detect simulated 'air–water void' defects within insulation layers up to 50 mm in depth, with a measurement sensitivity at the 10⁻4 pF level. The integrated system offers a robust, cost-effective, and non-invasive solution for the early warning of CUI, addressing critical limitations of existing NDT techniques and paving the way for intelligent pipeline integrity management.

Keywords Insulated pipelines, Corrosion under insulation (CUI), Capacitive sensor, Non-destructive testing, Automated classification

As a key type of insulated pipelines, long-distance thermal pipelines serve as the core infrastructure of global centralized heating systems, enabling the efficient and stable long-distance transmission of high-temperature steam or hot water. As an energy-saving and environmentally friendly thermal energy transmission method, compared with decentralized heating, long-distance thermal pipelines can significantly reduce fossil energy consumption and pollutant emissions, providing critical support for the green transformation of new urban energy systems. Insulated pipelines represent the most reliable and efficient method for long-distance thermal transmission, offering stable guarantees for industrial process heat, commercial building heating, and residential domestic hot water supply. However, in harsh environments—such as frigid regions, high-humidity soil, or complex terrain sections—temperature fluctuations, erosion by soil corrosive media, and external force disturbances may lead to aging and damage of the pipeline insulation layer, failure of the protective structure, or corrosion of the pipeline itself, thereby compromising the structural integrity and operational safety of long-distance thermal pipelines. To mitigate these risks, anticorrosive and insulated long-distance thermal pipelines are widely adopted, whose composite anticorrosive and insulation layer can reduce heat loss along the way, block

[1]College of Mechanical and Electrical Engineering, China Jiliang University, Hangzhou 310018, China. [2]College of Metrology and Measurement Engineering, China Jiliang University, Hangzhou 310018, China. ✉email: zengtao806@sina.com

the intrusion of corrosive media, and ensure the energy efficiency and safety during transmission. Nevertheless, due to sealing defects of the insulation layer, mechanical damage to the outer protective pipe, or hidden defects during construction, the structural integrity of anticorrosive and insulated long-distance thermal pipelines is often impaired by corrosion under insulation (CUI). If left undetected, CUI may trigger catastrophic accidents such as thermal leakage and pipeline burst. Corrosion under insulation (CUI) refers to the electrochemical corrosion of the pipeline metal substrate beneath the anticorrosive and insulation layer. Owing to its extremely high concealment, wide impact range, and high repair costs, CUI has become a major technical challenge facing the thermal transmission industry. This phenomenon is difficult to detect through conventional testing methods; due to the obstruction by the composite insulation layer, traditional surface testing methods cannot directly detect the corrosion evolution process inside the insulation layer.

Multiple factors contribute to CUI, one of which is the unavoidable permeation of moist air into the pipeline insulation layer. Over extended periods, as ambient temperature fluctuates with seasonal changes—repeated cycles of "heating–cooling-heating–cooling"—the infiltrated moisture within the insulation layer undergoes continuous condensation and evaporation. This wet-dry cycle promotes the formation and expansion of air–water mixed cavities in the insulation. Eventually, these cavities come into contact with the innermost carbon steel pipe, initiating corrosion. Furthermore, defects or damage in the mechanical protective layer can provide pathways for water and ions to reach the metal surface, exacerbating corrosion. Across the entire thermal transmission industry, early detection of corrosion under insulation (CUI) plays a critical role in ensuring long-distance thermal insulated pipeline integrity management.

While non-destructive testing (NDT) is extensively employed for CUI inspection in thermal insulated pipelines, traditional NDT technologies face inherent limitations in such applications. Visual inspection is the most common and useful technology for CUI, but it requires stripping insulation material from areas with high corrosion potential to check the surface condition of the metal[1]. This results in visual inspection being the most expensive and time-consuming technology, as it is the only detection technique that requires the removal of insulation materials. Neutron backscatter technology is considered one of the fastest and most accurate detection strategies for detecting wet insulation in pipelines and containers. It mainly works by detecting the humidity on the insulation structure. The humidity of the insulation layer means that moisture has penetrated into the insulation layer and is reaching the steel pipe, causing CUI. One of the drawbacks of neutron backscatter technology is that it can only inspect small areas, and therefore cannot be used for inspecting long pipelines or large structures[2]. And the measuring device contains a radioactive source, which poses a safety risk to the operators. The pulse eddy current technology has been used to determine the wall thickness of pipelines. It requires placing a probe with a transmitting coil on the insulation structure. The coil will generate a magnetic field, causing magnetization of the tube wall. Afterwards, the current in the transmission coil can be turned off, which will cause a sudden decrease in the magnetic field and generate eddy currents that can be monitored by the probe. Due to the thickness of the corroded pipeline parts being different from normal, the diffusion of eddy currents through them will also be correspondingly different[3]. From the perspective of measurement principle, it is not easy to locate the cavity position of the insulation layer before corrosion occurs through eddy current technology. X-ray photography can be used to detect CUI, which uses imaging plates made of photoexcited phosphors. A cassette can be placed under the pipeline or container to be inspected, and then X-rays can be exposed to the insulation structure. Afterwards, the imaging board can be scanned by a laser scanner, which reads the image and digitizes it[4]. The structure of this technology is relatively complex, and the cost of measuring equipment is relatively high; The X-ray light source and imaging board are located on both sides of the tested pipeline, so it is necessary to reserve space on both sides of the pipeline in advance, which results in weak detection adaptability; And there are radiation safety hazards. Ultrasonic thickness measurement technology is considered one of the most expensive non-destructive testing technologies in CUI inspection, with usually accurate results, simple, fast, and universal technology. However, it has some limitations as it requires digging small holes in the protective layer and using an ultrasonic thickness gauge to measure the thickness of the insulation layer below the holes. It can only measure a small area below the holes, which may not necessarily be the area where CUI exists[5]. In addition, the small hole coverage required by this technology is prone to improper sealing, which may lead to more CUI[6]. Microwave detection technology utilizes microwaves as interrogation signals propagating along pipelines. This technology can study bent pipes, pipe supports, and different types of insulation materials[7]. However, the measurement system is complex and the cost of measurement equipment is relatively high.

Capacitive imaging (CI) is widely employed in various industrial applications due to its robustness, versatility, low cost, and high performance[8–14]. It operates by detecting possible changes in electrical properties near a CI probe equipped with coplanar electrodes, which typically consist of two or more metallic electrodes. In recent years, coplanar capacitive sensing has emerged as a promising electromagnetic NDT technique for addressing the limitations of traditional methods, especially in inspecting non-conductive, layered, and hybrid structures[15,16]. As a non-contact, radiation-free, and cost-effective approach, it leverages fringing electric field interactions with dielectric property variations to detect subsurface defects and moisture ingress—key precursors to CUI[17–21]. Recent studies have validated its efficacy in detecting defects through insulation layers: Abdollahi-Mamoudan et al. demonstrated via finite element modeling (FEM) and experiments that coplanar capacitive sensors can identify surface features of conductive materials covered by insulating layers, providing a theoretical and experimental basis for CUI-related defect detection[17].

Despite the progress made, existing capacitive sensors still suffer from rigid designs, limited adaptability to variable curvatures, and insufficient depth-resolution capability for detecting early-stage defects when applied to pipeline inspection. For instance, conventional capacitive sensors struggle to conform to the layered and curved surfaces of insulated pipelines and exhibit poor sensitivity to corrosion under insulation (CUI). Specifically,

although conventional array-based capacitive probes are effective for flat surfaces, they fail to maintain a uniform equidistance between electrodes and curved pipeline surfaces, resulting in signal drift and false alarms.

This study proposes a curvature-adaptive flexible array capacitive sensing scanning method for insulation layer defect detection, offering a novel solution for early warning of CUI in long-distance thermal insulated pipelines. Unlike conventional rigid capacitive probes, this innovative design integrates a soft elastomer substrate with arrayed capacitive sensors, enabling dynamic adaptation to cylindrical surfaces with varying radii of curvature for conformal measurements. This improves the signal-to-noise ratio and detection accuracy for insulation layer defects in cylindrical pipelines. Based on selectively activating different electrode pairs and analyzing relative capacitance deviations, this study proposes a novel approach aimed at determining the depth of internal defects in thermal insulated pipelines. Furthermore, to achieve automatic identification of defects in the pipeline protective jacket, thereby reducing interference from surface defects on the non-destructive testing of internal defects, enhancing the reliability of internal defect recognition, this study optimizes a one-dimensional convolutional neural network algorithm and applies it to the automated pre-classification of pipeline protective jacket defects. The detection device features an integrated and lightweight design suitable for field deployment, enabling non-destructive real-time pipeline monitoring without the need for protective jacket removal—meeting critical industry requirements for non-invasive inspection. By addressing the limitations of existing non-destructive testing technologies, this work establishes a new paradigm for intelligent inspection technologies in the thermal transmission industry.

Flexible array capacitive sensor with continuously adjustable curvature and its measurement device

Flexible curved-surface capacitive array electrode sensor probe

Thermal insulated pipelines typically consist of three concentric layers from the inside out (cross-sectional structure is shown in Fig. 1:

Innermost layer The inner pipe (carrier pipe), made of high-strength steel grades such as X70 or X80.
Middle layer The insulation layer, usually composed of polyurethane foam or a polyurethane-aerogel composite.
Outermost layer The protective jacket, generally made of high-density polyethylene (HDPE)."

For test objects with curved surfaces and multi-layer internal structures such as insulated pipelines, the capacitive sensor probe is designed as a flexible curved probe with adjustable curvature. Most insulated pipelines have diameters within 1 m and exhibit significant surface curvature. When traditional flat capacitive sensors are used to detect surface or internal defects, a substantial portion of the electric field is distributed in the space between the capacitive electrode and the curved surface of the test object. This results in a significant weakening of the "useful" electric field that actually penetrates into the test object. Particularly when the test object has a multi-layer internal structure, the attenuation of this "useful" electric field is more likely to prevent the sensor from detecting internal defects. If a flexible probe with a similar surface curvature is used for pipeline defect detection, the spatial dissipation of the electric field can theoretically be greatly reduced. The penetration performance of the electric field at the interfaces of heterogeneous multi-layer structures is relatively strong, which will enhance the strength of the effective capacitive signal, improve the sharpness of defect images, and increase the signal-to-noise ratio. The surface of the capacitive probe designed in this study allows continuous curvature adjustment via a threaded mechanism, making it adaptable to most curved test objects.

On the other hand, a single large-area capacitive metal electrode is prone to plastic deformation when bent, which can damage the electrode. In contrast, the array electrode design in this study enables extensive continuous bending deformation of the entire probe surface. This is because each electrode unit in the array has a relatively small area (15 mm × 4 mm), making it less susceptible to plastic deformation when the probe surface is bent.

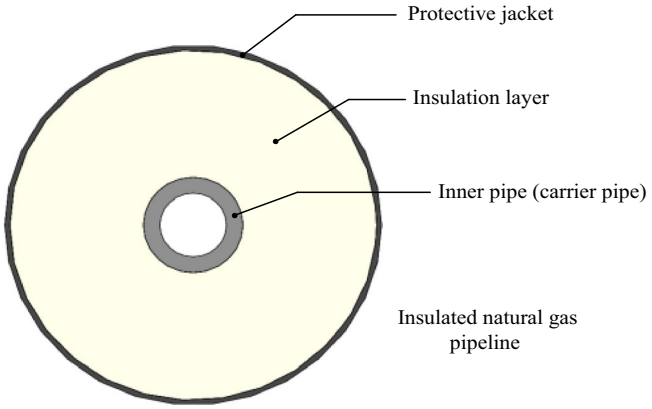


Fig. 1. Cross-sectional structure of the onshore insulated pipelines which typically consist of three concentric layers from the inside out.

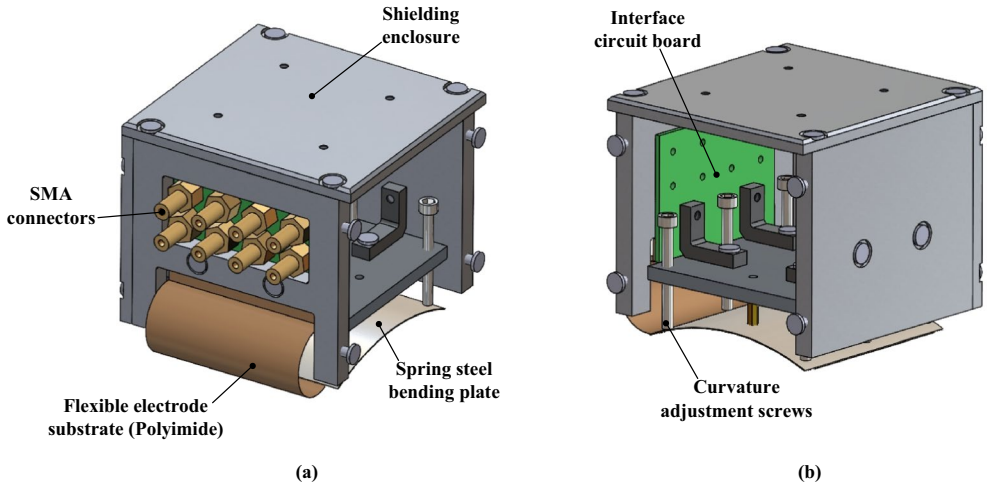


Fig. 2. The probe is primarily composed of a capacitive electrode array, a flexible electrode substrate, a spring steel curved deformation plate, an adjustable curvature screw set, a capacitance measurement interface circuit board, and an electromagnetic shielding housing. Subfigures (**a**) and (**b**) in the figure depict two perspective views of the capacitive sensor probe, which are mutually orthogonal at 90° in the horizontal plane.

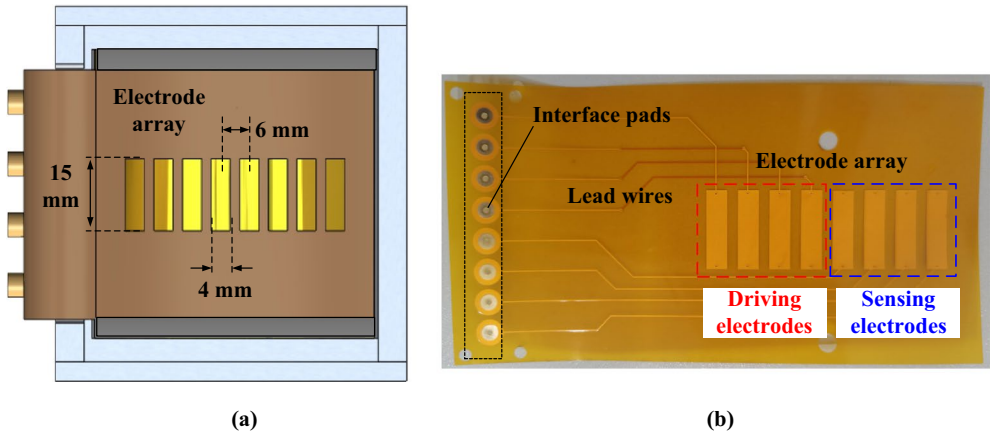


Fig. 3. The capacitive electrode array consists of multiple pairs of coplanar electrodes in a "drive electrode vs. sense electrode" configuration. Subfigure (**a**) depicts the position of the capacitive electrode array within the capacitive sensor probe as well as its relevant dimensional information, and Subfigure (**b**) shows a physical photograph of the capacitive electrode array.

The specific structure of the capacitive probe is shown in Fig. 2. The probe primarily consists of a capacitive electrode array, a flexible polyimide electrode substrate, a spring steel curved deformation plate, a set of curvature adjustment screws, a capacitive measurement interface circuit board, and an electromagnetic shielding enclosure. The capacitive electrode array comprises four pairs of coplanar electrodes in a "drive electrode vs. sense electrode" configuration, made of copper, as shown in Fig. 3. The primary rationale for adopting a rectangular electrode configuration in this study is that rectangular electrodes offer the highest area utilization efficiency when arranged in an array, and a larger effective electrode area enables the excitation of a stronger fringing electric field under the same operating voltage. The flexible substrate is fixed to a spring steel curved deformation plate, and the curvature of the spring steel plate is adjusted via a set of curvature adjustment screws to achieve conformal measurements on insulated pipelines with different radii. The capacitance measurement interface circuit board is responsible for connecting the electrode array to the backend capacitive measurement bridge. The probe features a semi-enclosed electromagnetic shielding housing designed to mitigate the impact of external stray electromagnetic interference on capacitance measurements. Coplanar capacitive electrodes represent an electrode design where all electrodes are arranged on the same plane. Compared to traditional parallel-plate capacitive designs, this configuration eliminates the need for electrodes on both sides of the sample, significantly enhancing measurement adaptability. Particularly for test objects with considerable thickness, such as insulated pipelines, the coplanar design avoids the issue of weak detection signals caused by severe electric field attenuation, thereby offering distinct measurement advantages in such scenarios.

Conventional parallel-plate capacitors generate a uniform bulk electric field between two opposing electrodes under the ideal condition (electrode spacing << electrode area), which is suitable for thin and flat sample detection but limited in penetrating layered and curved structures like insulated pipelines. In contrast, coplanar capacitive electrodes (drive-sense configuration) rely on the fringing field (or fringing capacitance) for non-destructive testing, where the electric field lines diverge from the drive electrode to the sense electrode in a non-uniform arc-shaped distribution (shown in Fig. 4). The fringing field exhibits a stratified intensity distribution along the depth direction, with higher field density in the near-surface region and gradual attenuation with increasing depth, which is the key physical basis for the defect depth detection in this study. This coplanar design eliminates the need for opposing electrodes on the tested sample, significantly enhancing the measurement adaptability for thick, layered insulated pipelines.

The coplanar capacitive probe scans the test object and reveals its surface or internal features through capacitance data curves or images. An AC voltage is applied to the probe during scanning, with the frequency carefully selected to avoid excessive magnetic field coupling and energy dissipation via electromagnetic radiation, which would degrade signal strength and signal-to-noise ratio (SNR). As the probe scans the sample's features, the electric field distribution becomes locally distorted due to variations in permittivity or conductivity, accordingly, the coupling capacitance of the probe changes.

Shielding measures

When a capacitive probe scans and inspects insulated pipelines, the external environment typically contains electromagnetic noise and possibly external electrostatic fields, both of which can interfere with capacitive detection. To protect the capacitive scanning measurements from the influence of external electromagnetic noise and electrostatic fields, this study first proposes a solution involving the design of a shielding shell (see Fig. 2). The shielding shell, made of aluminum alloy and grounded, encloses the coplanar capacitor in space, exposing only the front side of the capacitive electrode array. This blocks most electromagnetic waves and external electrostatic fields. Secondly, to mitigate potential capacitive coupling between the capacitive electrode and the shielding shell, which is inversely proportional to the coupling distance, the distance between the capacitive electrode and the directly opposing shielding shell is designed to be as large as possible while ensuring the overall compact size of the capacitive probe. Currently, this distance is set at 60 mm.

Composition of the scanning measurement system

The entire scanning measurement system primarily consists of a capacitive measurement probe, a capacitance bridge, hardware circuits, and a rotary scanning mechanical device, as illustrated in Fig. 5. A precision capacitance bridge, specifically the Tonghui TH283X series compact LCR digital bridge, is employed to monitor changes in the capacitance of the coplanar capacitor in real time. This bridge supplies an AC voltage to the coplanar capacitor of the probe to generate a fringing electric field. A coaxial cable is used to connect the drive electrode of the coplanar capacitor to the H terminal of the bridge, the sensing electrode to the L terminal, and all shields within the probe to the analog ground of the bridge. The capacitance bridge uploads the real-time collected capacitance measurement data to a computer via a USB data bus for data storage and automatic dynamic plotting.

The hardware circuits mainly include the signal interface circuit within the probe and the array channel switching circuit. The signal interface circuit is primarily used to extract signals from the capacitive electrodes. The array channel switching circuit enables the selection and switching of different electrodes in the array, after which the measurement signals are transmitted to the precision capacitance bridge via coaxial shielded cables for capacitance measurement.

A rotary scanning mechanical device is designed to drive the capacitive array probe to perform circumferential scanning inspections around the insulated pipeline being measured, as shown in Fig. 6. This device mainly consists of three sets of stepper motor-driven Mecanum wheels, a spring preload mechanism, and a frame mechanical structure. The oblique roller design of the Mecanum wheels ensures the mobility flexibility and omnidirectional movement capability of the rotary scanning mechanical device. The spring preload mechanism serves to press the scanning device against the surface of the insulated pipeline without interfering with the rotary scanning motion.

Method for determining the depth of internal defects

In the field of non-destructive testing (NDT), accurately determining the depth of hidden defects holds critical significance for multiple reasons. The depth of a defect may directly influence its threat to structural integrity.

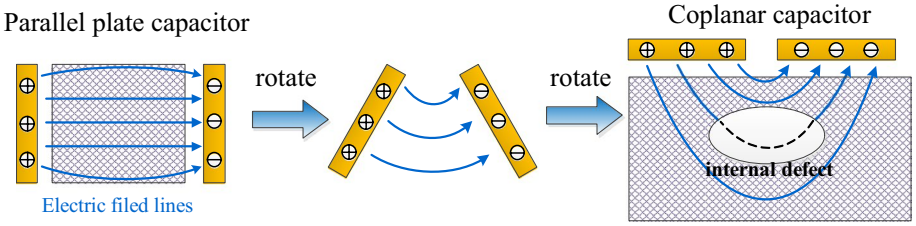


Fig. 4. Coplanar capacitive electrodes rely on the fringing field for non-destructive testing, where the electric field lines diverge from the drive electrode to the sense electrode in a non-uniform arc-shaped distribution.

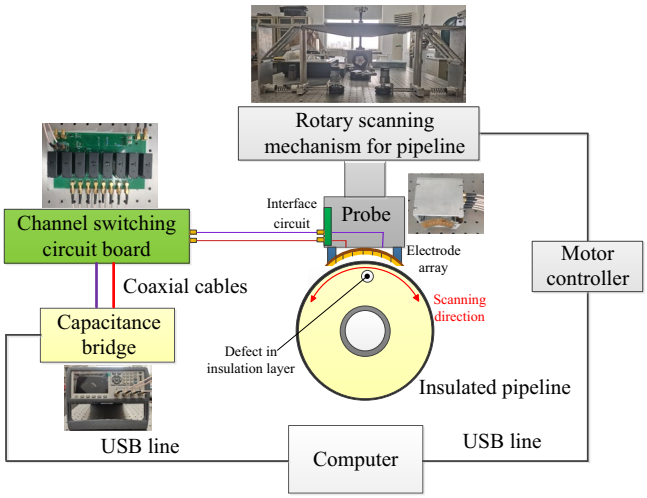


Fig. 5. The scanning measurement system is primarily composed of a capacitive measurement probe, a capacitance bridge, hardware circuits, and a rotary scanning mechanical device.

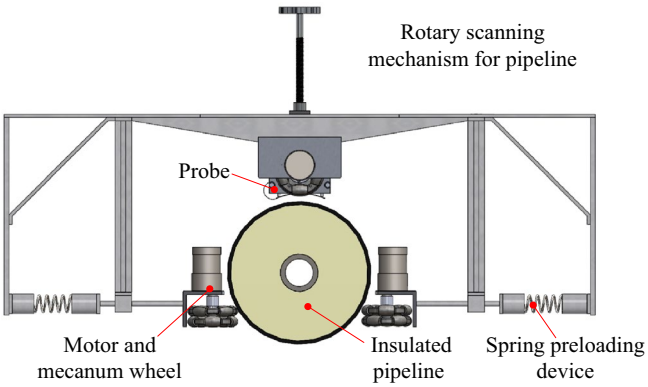


Fig. 6. A rotary scanning mechanical device, designed to drive the capacitive array probe for circumferential scanning detection around the insulated pipeline under test.

And precise depth information can guide maintenance strategies, reducing over-maintenance (e.g., avoiding unnecessary wholesale replacements) or under-maintenance (e.g., missing deep defects leading to rework), thereby significantly lowering maintenance costs. However, current capacitive sensing measurements for CUI primarily focus on detecting the presence of internal defects, their two-dimensional locations, and their sizes, but do not precisely resolve the depth information of these defects. Based on finite element simulation analysis, this study focuses on the relative deviation of capacitance values among all electrode pairs in the capacitive electrode array, proposing a novel approach aimed at determining the depth of internal defects in thermal insulated pipelines.

First, the electric field distribution generated by a capacitive electrode array with six electrode pairs was simulated using the electromagnetic finite element analysis (FEA) software ANSYS Maxwell (a dedicated tool for low-frequency electromagnetic simulation, originally developed by Ansoft Corporation and now integrated into the ANSYS simulation suite). The simulation results are shown in Fig. 7. The electrode pairs in the array, from innermost to outermost, are labeled as Pair 1 to Pair 6. Analysis of the simulation results reveals that the edge electric field generated by the capacitive electrode array exhibits a “stratified characteristic” along the depth direction.

Second, through electrostatic field simulations, the changes in capacitance values of the electrode array were acquired when a near-spherical void (representing the simplest defect scenario) was present at various depths within the insulation layer of a pipeline. The FEA model of this simulation is shown in Fig. 8. The insulation material was set as polyurethane foam with a relative permittivity of 1.8. For a near-spherical void, which often contains a mixture of moisture and air due to prolonged water vapor condensation, the relative permittivity was set to 10, a value between air and water.

Using the capacitance values of each electrode pair in the defect-free case as the control group, and the capacitance values when the defect was located at various depths as the measurement group, the relative deviation in capacitance for each electrode pair was calculated by dividing the difference between the two by the

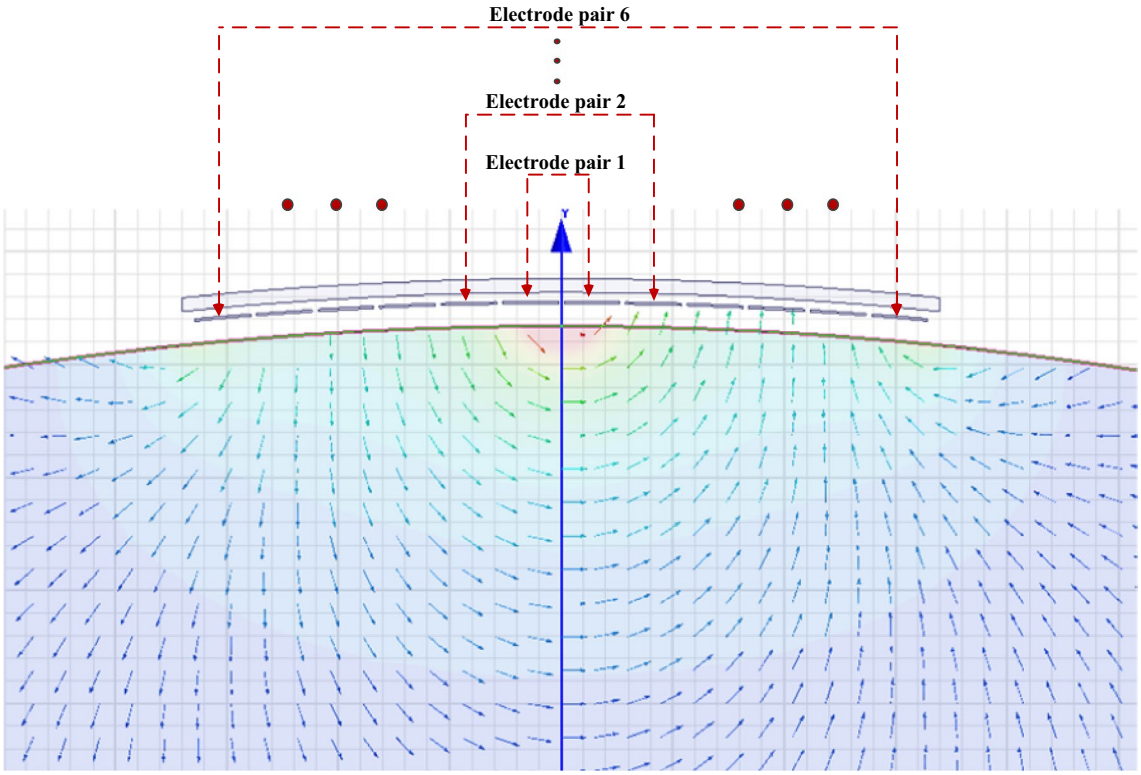


Fig. 7. The electric field distribution generated by the capacitive electrode array exhibits a "stratified characteristic" along the depth direction.

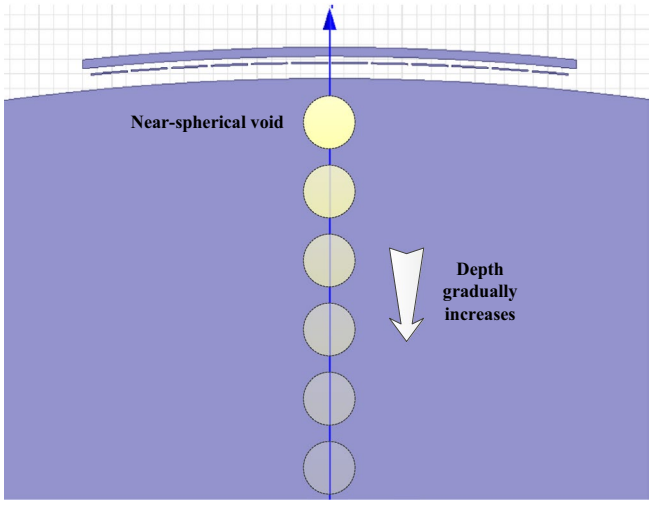


Fig. 8. Changes in capacitance values of the electrode array were acquired through electrostatic field simulations when a near-spherical void was present at various depths within the insulation layer of a pipeline.

control group value. The simulation results are recorded in Table. 1. By analyzing these results, the relationship between defect depth and the relative deviation in capacitance for each electrode pair was plotted in Fig. 9 . The analysis revealed that as the depth of the void increased, the electrode pair number corresponding to the maximum relative capacitance deviation also increased, indicating that the electrode pair detecting the peak relative deviation shifted outward. This confirms the performance characteristic that "the edge electric fields generated by different electrode pairs in the array, from innermost to outermost, exhibit a stratified distribution along the depth direction." Based on this characteristics, forward application can determine the approximate depth range of potential internal defects within the insulation layer, while reverse application can utilize specific electrode pairs in the array to scan and detect internal defects at targeted depths within the insulation layer.

Defect depth	Electrode pair number	Measurement group C_1	Control group C_0	Capacitance deviation $\triangle = C_1 - C_0$	Relative capacitance deviation $\triangle / C_0$
4 mm	1	29.330 pF	28.555 pF	0.775 pF	**2.714%(max)**
	2	13.374 pF	13.101 pF	0.273 pF	2.084%
	3	9.523 pF	9.398 pF	0.125 pF	1.330%
	4	7.639 pF	7.570 pF	0.069 pF	0.911%
	5	6.432 pF	6.389 pF	0.043 pF	0.673%
	6	5.493 pF	5.465 pF	0.028 pF	0.512%
8 mm	1	28.704 pF	28.555 pF	0.149 pF	0.522%
	2	13.227 pF	13.101 pF	0.126 pF	**0.962%(max)**
	3	9.477 pF	9.398 pF	0.079 pF	0.841%
	4	7.621 pF	7.570 pF	0.051 pF	0.674%
	5	6.423 pF	6.389 pF	0.034 pF	0.532%
	6	5.488 pF	5.465 pF	0.023 pF	0.421%
12 mm	1	28.602 pF	28.555 pF	0.047 pF	0.165%
	2	13.159 pF	13.101 pF	0.058 pF	0.443%
	3	9.446 pF	9.398 pF	0.048 pF	**0.511%(max)**
	4	7.605 pF	7.570 pF	0.035 pF	0.462%
	5	6.415 pF	6.389 pF	0.026 pF	0.407%
	6	5.484 pF	5.465 pF	0.019 pF	0.348%
16 mm	1	28.576 pF	28.555 pF	0.021 pF	0.074%
	2	13.132 pF	13.101 pF	0.031 pF	0.237%
	3	9.428 pF	9.398 pF	0.03 pF	0.319%
	4	7.596 pF	7.570 pF	0.026 pF	**0.343%(max)**
	5	6.410 pF	6.389 pF	0.021 pF	0.329%
	6	5.481 pF	5.465 pF	0.016 pF	0.293%
20 mm	1	28.567 pF	28.555 pF	0.012 pF	0.042%
	2	13.119 pF	13.101 pF	0.018 pF	0.137%
	3	9.418 pF	9.398 pF	0.02 pF	0.213%
	4	7.589 pF	7.570 pF	0.0185 pF	0.244%
	5	6.405 pF	6.389 pF	0.016 pF	**0.250%(max)**
	6	5.478 pF	5.465 pF	0.013 pF	0.238%
24 mm	1	28.562 pF	28.555 pF	0.007 pF	0.025%
	2	13.113 pF	13.101 pF	0.012 pF	0.092%
	3	9.412 pF	9.398 pF	0.014 pF	0.149%
	4	7.584 pF	7.570 pF	0.014 pF	0.185%
	5	6.402v	6.389 pF	0.013 pF	**0.203%(max)**
	6	5.475 pF	5.465 pF	0.01 pF	0.183%
28 mm	1	28.560 pF	28.555 pF	0.005 pF	0.018%
	2	13.109 pF	13.101 pF	0.008 pF	0.061%
	3	9.407 pF	9.398 pF	0.009 pF	0.096%
	4	7.580 pF	7.570 pF	0.01 pF	0.132%
	5	6.398 pF	6.389 pF	0.009 pF	0.141%
	6	5.473 pF	5.465 pF	0.008 pF	**0.146%(max)**

Table. 1.. Using the capacitance values of each electrode pair in the defect-free case as the control group, and the capacitance values when the defect was located at various depths as the measurement group, the relative deviation in capacitance for each electrode pair was calculated.

It should be noted that to truly achieve the accurate determination of the depth of internal defects in the insulation layer, it is necessary to obtain practical defect samples with different depths in thermal insulated pipelines and conduct calibration experiments for the depth-relative capacitance deviation. Given the current difficulty in acquiring practical defect samples with multiple depths, this study currently focuses on proposing a novel approach for determining the depth of internal defects, and calibration experiments using practical samples will be conducted in subsequent studies.

Decoupling method for characteristic aliasing between protective jacket surface topography defects and internal insulation layer defects

Due to limitations in the actual injection molding process, the cylindricality of the outermost protective jacket of insulated pipelines is often imperfect, resulting in irregular micro-scale protrusions or depressions on the

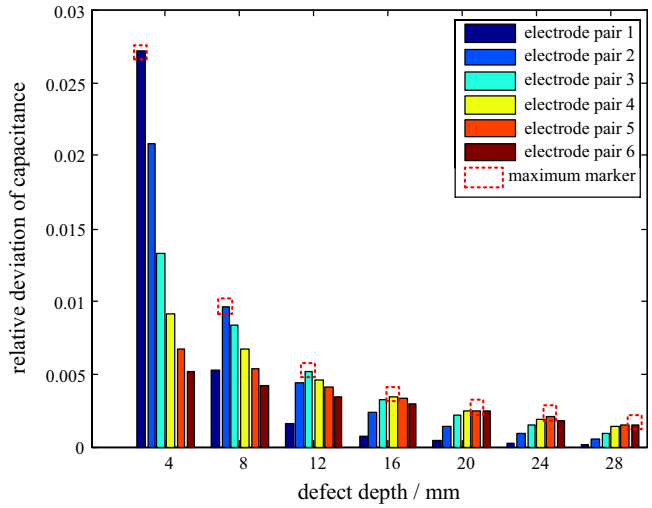


Fig. 9. As the depth of the void increased, the electrode pair number corresponding to the maximum relative capacitance deviation also increased.

jacket surface. When using capacitive probes to detect internal defects within the insulation layer, the surface topography defects of the protective jacket cause characteristic aliasing with internal insulation layer defects. Under this condition, it becomes extremely difficult to distinguish whether amplitude variations in the capacitive detection curve originate from internal defects or surface defects of the protective jacket.

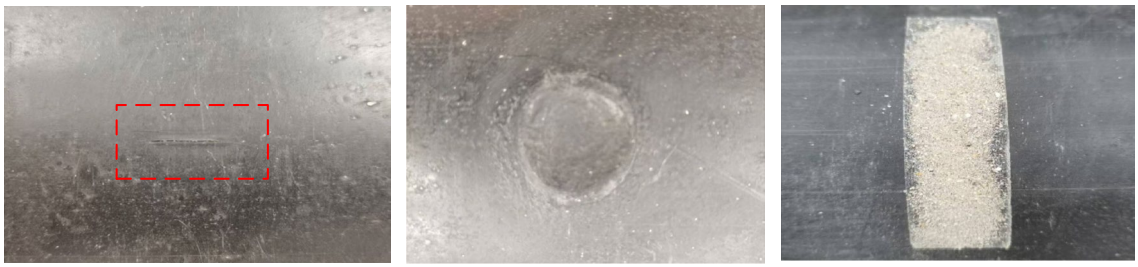
Based on the difference in the attenuation efficiency of capacitive measurement sensitivity between surface topography defects of the protective jacket and internal defects of the insulation layer, this study proposes a decoupling method by varying the lift-off height (the distance between the capacitive electrode and the protective jacket surface). Adjusting the lift-off height alters the capacitive measurement sensitivity for both types of defects. The optimal lift-off height is determined through experiments to achieve decoupling of the two defect features. The core principle of the feature decoupling method is as follows: as the lift-off height increases, the capacitive detection sensitivity for both surface defects of the protective jacket and internal defects of the insulation layer decreases. However, the sensitivity reduction for surface defects is more significant than for internal defects, which is beneficial for detecting internal defects. Conversely, if the lift-off height is excessively increased, the sensitivity for detecting internal defects may drop to an excessively low level, adversely affecting detection accuracy and efficiency. This represents a trade-off problem.

To address this, we propose a method to determine the optimal lift-off height: gradually increase the lift-off height until the amplitude variation in the detection curve caused by surface defects of the protective jacket just disappears. At this point, the distinguishability between the characteristic information of internal defects and that of surface defects is maximized. This achieves both decoupling of the two defect features and maximization of the internal defect detection signal, making this lift-off height optimal. It is important to note that during the gradual increase of the lift-off height, the amplitude of the internal defect signal must remain above the noise level of the capacitive scanning curve to ensure measurement validity. The detailed experimental procedure will be elaborated in Section "Decoupling for feature aliasing between protective jacket defects and insulation defects based on the lift-off height".

Automated recognition of surface defects on insulated pipeline jackets via an enhanced 1D CNN algorithm

The presence of defects on the protective jacket surface (mainly including 1. cracks, 2. corrosions, and 3. accumulated sand/dust coverage, as shown in Fig. 10) can interfere with the testing results of internal defects. For small-area surface defects or those with low height variation, the method described in Section "Decoupling method for characteristic aliasing between protective jacket surface topography defects and internal insulation layer defects" for determining the optimal lift-off height can be used to decouple the aliasing of features between the jacket topography and internal insulation layer defects. However, for large-area defects or those with significant height variation, the aforementioned method may not achieve complete decoupling. In such cases, it is necessary to automatically identify the condition of the protective jacket surface to distinguish and determine the true source of variation in the capacitive scanning signal—i.e., whether the capacitive change originates from an insulation layer defect or a jacket defect. Automatically recognize surface defects helps reduce the probability of misclassifying defect types and can also assist in evaluating the effectiveness of the protective jacket's functional properties (e.g., moisture resistance and mechanical protection).

First, leveraging the difference in the attenuation efficiency of capacitive measurement sensitivity between surface defects and internal insulation defects, the lift-off height between the capacitive electrode and the protective jacket surface is minimized (set to approximately 1 mm in actual measurements) to maximize the sensitivity of the capacitive measurement to surface topography defects. Under these conditions, the amplitude of the capacitive change caused by internal defects is often much smaller than that caused by surface defects and



(a) crack (b) corrosion pit (c) accumulated sand/dust

Fig. 10. Three most common types of defects on insulated pipeline protective jackets.

is essentially masked by the latter. Second, machine learning algorithms are employed to automatically classify the types of surface defects.

Dataset establishment

To enable intelligent recognition of the three main defect types, a sample database must be established. We created the three defect types on pipeline protective jackets in the laboratory and acquired defect samples through capacitive scanning. The result of a single capacitive scan is a one-dimensional curve, meaning the sample data type is a one-dimensional array. In this study, 400 samples of four types of actual physical defects were collected. Through data augmentation techniques—including adding moderate noise, random scaling, random shifting, and random segment reversal—the sample size was expanded to 4000. This included: 1000 control samples with no defects, 1000 crack samples, 1000 corroded pit samples, and 1000 sand/dust accumulation samples. To prevent model overfitting and enhance generalization, the dataset must exhibit sufficient diversity. Thus, the crack samples encompassed features of varying lengths, depths, and scanning directions; the corrosion defect samples had different contour shapes, diameters, and depths, and included variations in the scanning path across the corroded pits. The aforementioned data augmentation techniques further increased sample diversity.

Intelligent machine learning recognition algorithm

To achieve automatic identification of surface defects on the protective jackets, a 1D convolutional neural network (1D-CNN) algorithm from machine learning was adopted. In preliminary experiments, we found that the capacitive scanning curves corresponding to cracks and corroded pits were nearly indistinguishable based on shallow features (e.g., amplitude of peaks/troughs, width, average slope of rising/falling edges), as shown in Fig. 11. This is because surface defects are often accompanied by minor secondary defects (e.g., slight surface undulations, uneven jacket thickness, or embedded impurities), preventing the "shallow features" of the scanning curves from forming stable mappings with the defects themselves. Therefore, we employed a 1D-CNN algorithm, improved based on actual performance, to mine "deep features" within the scanning curves. These deep features were mapped to the types of protective jacket surface defects, constructing a corresponding 1D-CNN model for automatic identification of defect types.

A convolutional neural network (CNN) is a deep learning architecture specifically designed for processing grid-like data. Its core operations involve automatic local feature extraction via convolutional layers and dimensionality reduction via pooling layers to enhance computational efficiency and robustness. A 1D-CNN is a variant of CNN where the convolutional kernel slides along a single dimension, making it suitable for sequential data. Since the measurement data in this study is one-dimensional sequential data, a 1D-CNN was adopted. The 1D-CNN can automatically extract meaningful and discriminative local patterns or feature segments from raw signals. The network architecture of the 1D-CNN was implemented in VS Code software.

Algorithm improvement and testing verification

The network architecture of the improved 1D-CNN algorithm is shown in Fig. 12. This architecture consists of an initial convolutional layer, two multi-scale feature fusion modules (each containing three parallel convolutional layers with different kernel sizes, a batch normalization layer, a ReLU activation layer, and a channel attention mechanism), a deep feature extraction module (containing two convolutional layers, two batch normalization layers, two ReLU activation layers, and two max-pooling layers), and a classification head (comprising a global average pooling layer, a fully connected layer, and a dropout layer). It processes one-dimensional grayscale curve data of length 300 as input, extracts features through the multi-scale feature fusion modules and channel attention mechanism, and outputs recognition results for the four types of defects on the insulated pipeline protective jacket.

Regarding algorithm improvement and optimization, this study primarily implemented two types of measures:

First, a series of steps were taken to prevent model overfitting. Model overfitting occurs when a model performs too well on the training data, learning the "noise" and "specific details" rather than the "underlying general patterns," leading to poor performance on new, unseen data—i.e., poor generalization ability. To suppress overfitting, the following measures were implemented: data augmentation, dropout layers, early stopping, batch normalization, and learning rate scheduling.

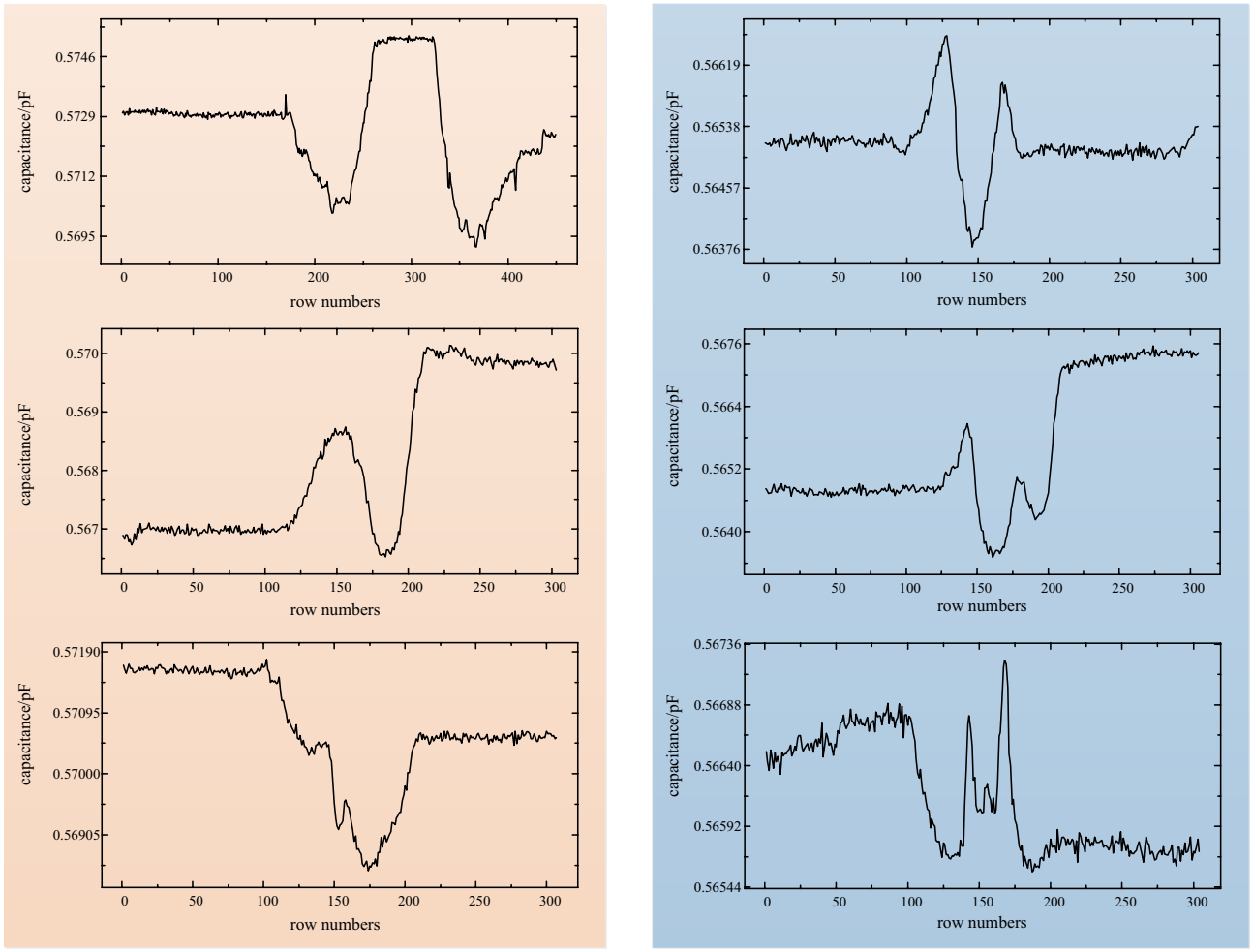


Fig. 11. Scanning measurement curves of 3 crack samples and 3 corrosion pit samples. It is nearly impossible to distinguish between cracks and corrosion pits based on "shallow features" of the curves (e.g., amplitude of peaks/troughs, width, average slope of rising/falling edges).

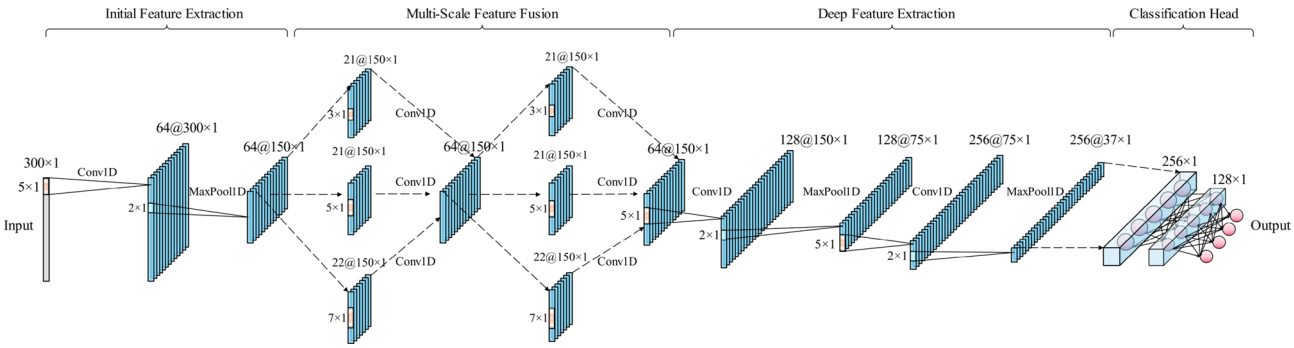
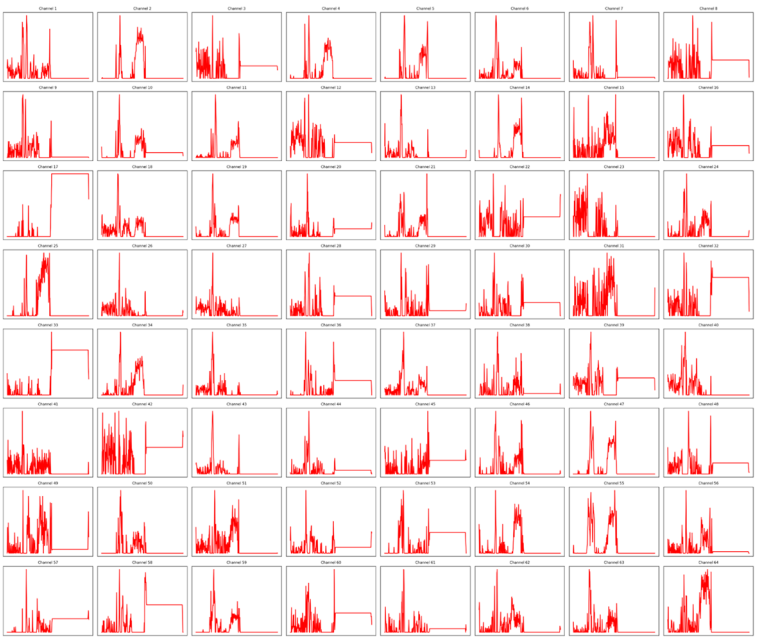


Fig. 12. Network architecture of the improved 1D-CNN algorithm.

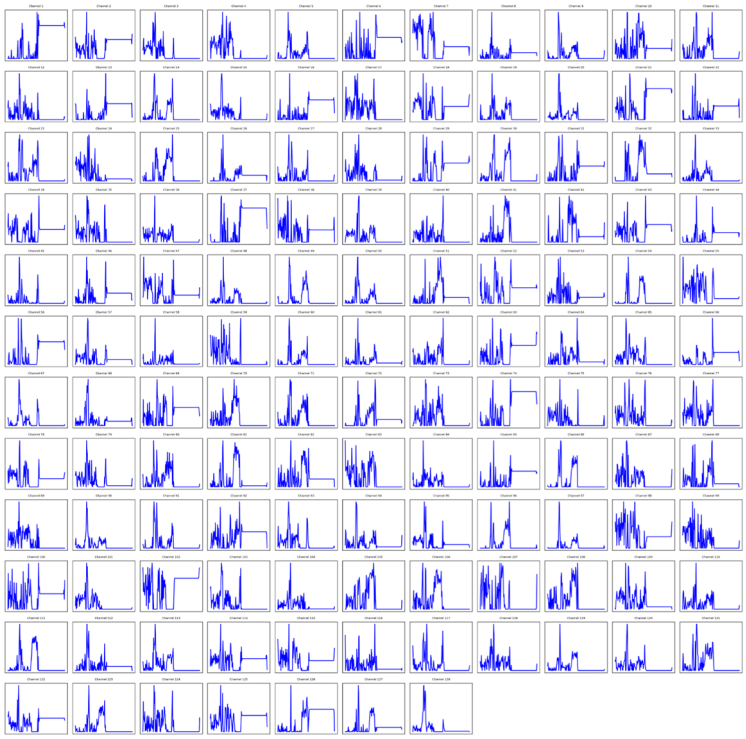
Second, to enhance the model's feature recognition capability, the core algorithm combines multi-scale feature fusion with a channel attention mechanism. The network first extracts basic features through an initial convolutional layer, then uses two multi-scale feature fusion modules to extract features at different receptive fields in parallel using convolutional kernels of sizes 3, 5, and 7, as shown in Fig. 12. A channel attention mechanism adaptively enhances the weights of important feature channels, which avoids the core features of defects being masked by irrelevant interference features. This design enables the model to capture both local

subtle features and global information of jacket defects, significantly improving the ability to distinguish between similar defects. Additionally, a hybrid loss function combining cross-entropy and focal loss was introduced to further alleviate class imbalance issues in the defect samples, making the model focus more on hard-to-classify defect samples.

To test the accuracy of the improved 1D-CNN algorithm, 60%, 20% and 20% of the samples in Dataset were randomly selected as training, validation and test sets. The deep features are extracted in each convolutional layer, with the extraction results of the first two layers shown in Fig. 13. The test results are shown in Table 2.



(a) extraction 1



(b) extraction 2

Fig. 13. Deep features extracted in the first two convolutional layers.

	Precision	Recall	F1-score	Support
Normal	0.9346	1.0000	0.9662	200
Crack	0.9563	0.9850	0.9704	200
Corrosion	1.0000	0.8900	0.9418	200
Sand	0.9851	0.9950	0.9900	200

Table. 2. Model test results.

		Normal	Crack	Corrosion	Sand
F1-score	Test 1	0.935	0.924	0.971	0.961
	Test 2	0.961	0.951	0.969	0.969
	Test 3	0.953	0.949	0.959	0.964
	Test 4	0.964	0.952	0.971	0.969
	Test 5	0.972	0.955	0.966	0.977
	Test 6	0.946	0.934	0.969	0.977
	Test 7	0.961	0.949	0.973	0.982
	Test 8	0.961	0.944	0.964	0.977
	Test 9	0.945	0.926	0.964	0.972
	Test 10	0.950	0.932	0.969	0.975
	SD	± 0.011	± 0.011	± 0.004	± 0.006

Table. 3. Validating the robustness of the network model during random splits of the training/test sets.

Models	Accuracy	F1-score
RF	0.9375	0.9380
MLP	0.2500	0.1000
LSTM	0.9000	0.9028
1DCNN	0.9675	0.9671

Table. 4. Analysis of comparative experiment results.

These results represent the performance metrics of a four-class model (normal, crack, corrosion, sand), with 200 test samples per class (balanced support). The three metrics reported are precision, recall, and F1-score. Precision is the proportion of correct predictions among all samples predicted as a certain class; Recall is the proportion of actual positives correctly identified; and F1-score is the harmonic mean of Precision and Recall, serving as the best single metric for overall model performance. As shown in Table. 2, the model achieves high overall accuracy, indicating that the algorithm can intelligently and accurately identify the three defect types.

Furthermore, to verify the robustness of the network model during random splits of the training/validation/test sets, the samples were randomly partitioned 10 times, and the classification performance for each test was recorded. The F1-score was used as the observation metric, and the results are shown in Table. 3, where SD is the standard deviation of the F1-scores from the 10 tests. The differences between the 10 test results are minimal: the standard deviation for the "normal" and "crack" classes is approximately 1%, while for the "corrosion" and "sand" classes, it is even smaller, on the order of 0.1%. This demonstrates that the network model established in this study possesses strong robustness.

Comparison experiments

To comprehensively evaluate the detection performance of the proposed 1DCNN model in the defect classification task for insulated pipes, comparative experiments were conducted on the time-series curve dataset of defects by selecting traditional machine learning algorithms (random forest, RF; multilayer perceptron, MLP) and deep learning time-series models (long short-term memory network, LSTM), which are all typical baseline algorithms for processing one-dimensional time-series data. For the MLP model, the key tuned parameters include the size of hidden layers (64,32), initial learning rate (0.0005), and L2 regularization coefficient(0.01); for the RF model, we mainly optimized the maximum depth of individual decision trees (15) and the minimum number of samples required for node splitting (5); for the LSTM model, the main tuned parameters cover the number of neurons in core LSTM layers (64) and the number of neurons in fully connected layers (32). All models were optimized using cross-validation and grid search. The results are presented in the table. As shown in the Table. 4, deep learning models (1DCNN, LSTM) and the RF model among traditional machine learning algorithms achieved overall good performance, while only the MLP model was significantly inferior in both metrics. Specifically, as a representative traditional machine learning algorithm, the RF model achieved high

performance by virtue of the advantages of ensemble learning, with Accuracy and F1 reaching 0.9375 and 0.9380, respectively. The LSTM model, a classic deep learning model for time-series data, performed slightly worse than the RF model, with the two metrics being 0.9000 and 0.9028, respectively. In contrast, due to the loss of local sequence information caused by its fully connected structure, the MLP model exhibited obvious shortcomings in the time-series classification task, with an Accuracy of only 0.2500 and a F1 as low as 0.1000. Among all comparative models, the proposed 1DCNN model achieved the optimal performance in both accuracy and class balance (class balance here refers to the balance between Precision and Recall as reflected by the F1), with Accuracy and F1 reaching 0.9675 and 0.9671, respectively. Compared with the RF model, these two metrics were improved by approximately 3.20% and 3.10%, respectively; compared with the LSTM model, they were increased by about 7.50% and 7.12%, respectively.

Compared with the RF model, the 1DCNN model has greater advantages in capturing subtle defect patterns of time-series curves through an end-to-end multi-scale feature fusion mechanism. In contrast to the MLP model, the 1D convolutional structure of the 1DCNN model possesses an inherent local feature perception advantage, which can accurately capture the local structural correlations and subtle changes of time-series data. When compared with the LSTM model, the 1DCNN model integrates channel attention and dilated convolution modules (the dilated convolution modules introduce “holes” in the convolution kernel so the algorithm can capture the feature information of a longer section of the capacitive scanning curve at one time), which not only enhance the weights of key defect features but also expand the receptive field. This makes up for the deficiency of pure time-series models in capturing local high-frequency features, thus achieving superior comprehensive performance.

Experiments

Decoupling for feature aliasing between protective jacket defects and insulation defects based on the lift-off height

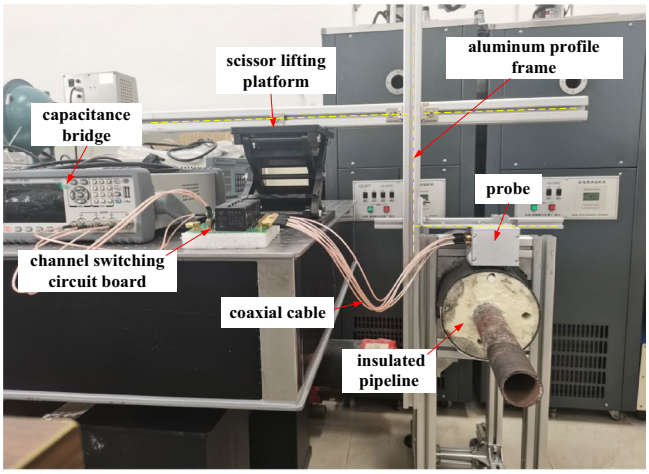
To decouple the aliasing of features between protective jacket topography defects and internal insulation layer defects, experiments were conducted based on the method proposed in Section "Decoupling method for characteristic aliasing between protective jacket surface topography defects and internal insulation layer defects" for determining the optimal lift-off height. An experimental setup with adjustable lift-off was constructed, as shown in Fig. 14. The capacitive probe was fixed to the end surface of a scissor lift platform via an aluminum profile frame and adapters. By adjusting the height of the scissor lift platform, the capacitive probe could be raised or lowered to control the lift-off height. Below the probe, the insulated pipeline sample was secured on another aluminum profile frame. The outer diameter of the pipeline was 226 mm, with a protective jacket thickness of 2 mm and an insulation layer thickness of approximately 60 mm. The capacitive scanned signals were transmitted via shielded coaxial cables to a channel-switching circuit board and then to a capacitive measurement bridge for data acquisition.

Internal defects in insulated pipelines primarily result from incomplete injection molding, with cavity defects often concentrated near the outer edge of the pipeline—i.e., in the shallow region close to the protective jacket. Therefore, during the process for determining the optimal lift-off height, the internal defects were positioned within the shallow region of the insulation layer. Specifically, defects were introduced at depths not exceeding one-third of the total insulation thickness. A cavity was excavated at the outer edge of the insulation layer to simulate a defect, and titanium dioxide (TiO_2) powder was inserted into the cavity as a substitute for an "air–water mixture." TiO_2 powder was selected due to its dielectric properties being similar to those of water: the relative permittivity of water at low frequencies typically ranges from 70 to 80, while that of TiO_2 powder ranges from 80 to 100.

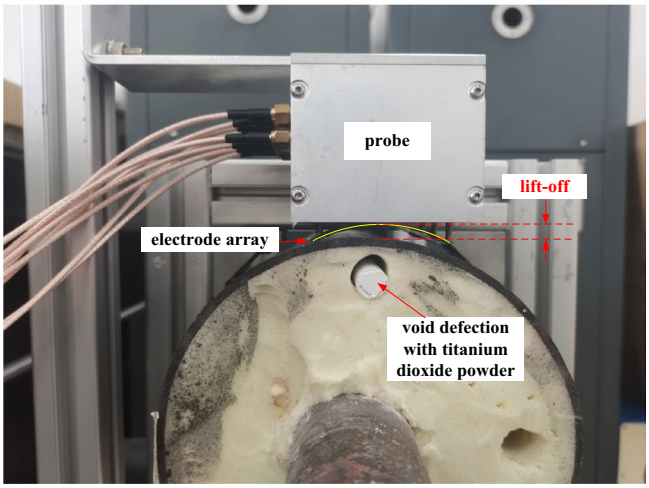
During the experiment, the lift-off height was incrementally increased from 0 to 1 mm in steps of approximately 0.2 mm using the scissor lift platform. Capacitive scanning was performed at six distinct lift-off heights to detect the void defect filled with TiO_2 powder. The results are shown in Fig. 15. From the curve family in Fig. 15a, two key observations can be made: first, the capacitance values gradually decreased with increasing lift-off height, which is consistent with fundamental capacitive principles; second, the features of jacket surface defects outside the void region became progressively weaker, while the “dip” feature corresponding to the void defect in the capacitive curves became increasingly prominent against this weakening background (see dashed box in Fig. 15a). This experimentally validates the property that "the attenuation efficiency of capacitive measurement sensitivity differs between surface topography defects of the protective jacket and internal defects of the insulation layer." When the lift-off height reached 1 mm, the features of jacket surface defects were nearly negligible in the scanning curves, while the void defect feature remained highly distinct (Fig. 15b). Moreover, the amplitude of the defect signal was significantly higher than the noise level of the scanning curves. Since further increasing the lift-off height would not further suppress jacket surface defect features but would instead reduce the amplitude of the cavity defect signal, the optimal lift-off height under these experimental conditions was determined to be approximately 1 mm.

Suppression of parasitic capacitance

During initial experimental testing, it was observed that in the capacitive scanning curve, an additional “abnormal” depression region appeared following the segment corresponding to the "air–water void" defect feature, as shown by the red curve in Fig. 16. This abnormal depression feature arises because the extended traces on the flexible substrate of the capacitive array are positioned extremely close to the surface of the insulated pipeline under test (as shown in Fig. 17a,b). Furthermore, the relatively large number of these traces (8 in total) introduces parasitic capacitance between the traces and the measured object, resulting in measurement errors in the scanning results.



(a)



(b)

Fig. 14. Experimental setup for decoupling feature aliasing between jacket topography defects and internal insulation defects: (**a**) overall view, and (**b**) close-up view of the probe and sample.

To address this issue, a soft shielded tape was applied to cover the extended trace sections on the substrate (as shown in Fig. 17c) and grounded to eliminate the measurement error. The shielded tape comprises a metallic conductive layer, a flexible insulating substrate, and an adhesive layer. Its flexible property enables adaptation to the bending deformation of the probe without impairing the curvature adjustment function. Specifically, the metallic conductive layer is made of aluminum, with a typical thickness of 10–30 μm and an electrical conductivity of $\sigma = 3.8 \times 10^7$ S/m (at 20℃), which guarantees reliable shielding performance and grounding conductivity. The flexible insulating substrate is polyimide, featuring a relative permittivity of $\varepsilon_r = 3.0–3.5$ (at a frequency of 1 kHz). After equipping the capacitive probe with the grounded shielding tape, capacitive scanning measurements were again performed on the insulated pipeline. The results, shown by the black curve in Fig. 16, demonstrate that covering the extended trace sections with the shielded tape effectively resolves the associated parasitic capacitance issue.

Mitigation of capacitive measurement noise and leakage current effects

Since the capacitance variation reflected in the capacitive scanning curve for "air–water void" defects within the insulation layer is only on the order of $4–6 \times 10^{-4}$ pF, effectively detecting such defects requires suppressing the noise level of the capacitive scanning curve to at least the 10^{-4} pF level. In addition to designing a well-shielded enclosure for the capacitive measurement probe, this work also ensures a high signal-to-noise ratio (SNR) for the capacitive signal by selecting the optimal operating frequency band for the capacitive bridge.

Experimental results revealed that the noise in the capacitive signal measured by the array electrode probe is primarily distributed in the low-frequency range (below 10 Hz), with a power spectral density approximately inversely proportional to frequency, indicating that the dominant source of noise is 1/f noise. And the preamplifier and subsequent signal conditioning circuits of the capacitance bridge are susceptible to generating 1/f noise. When the measurement system operates at low frequencies, the contribution of 1/f noise becomes substantial. To address this issue, we progressively increased the operating frequency of the capacitive bridge to identify

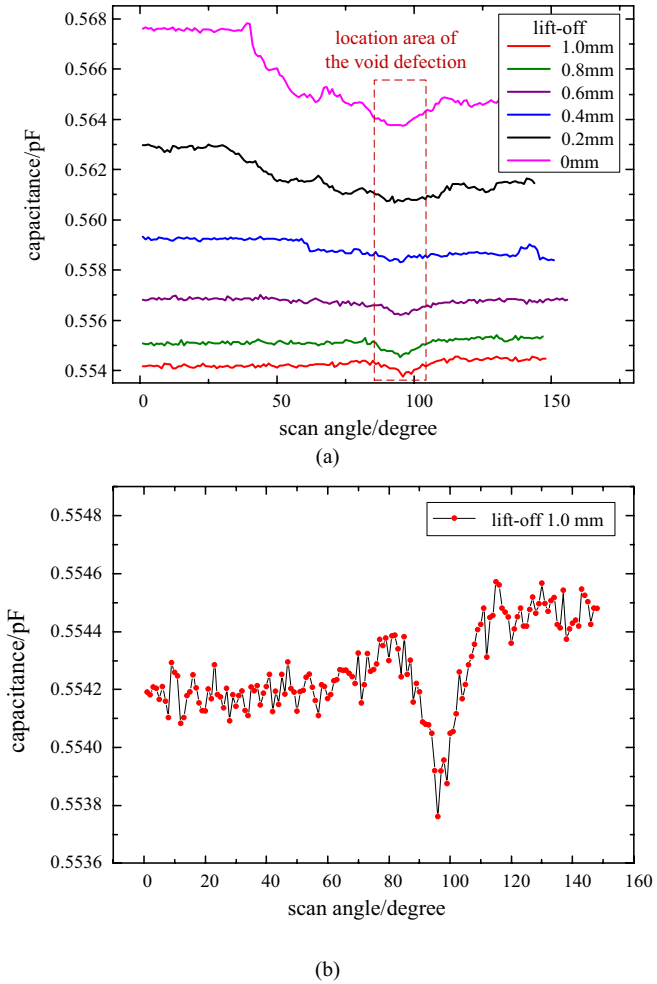


Fig. 15. Determination of the optimal lift-off height through calibration experiments. (**a**) Capacitive scanning results for a void defect filled with titanium dioxide (TiO_2) powder as the lift-off height was progressively increased from 0 to 1 mm. (**b**) Capacitive scanning curve obtained at a lift-off height of 1 mm.

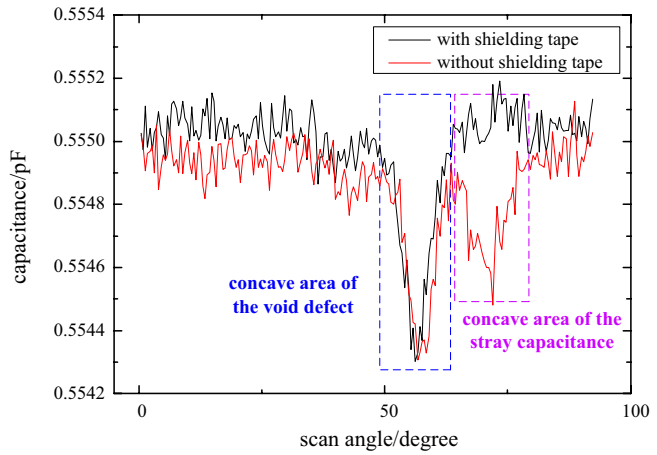


Fig. 16. Influence of parasitic capacitance caused by extended traces on the flexible substrate of the capacitive array on the capacitive measurement curve.

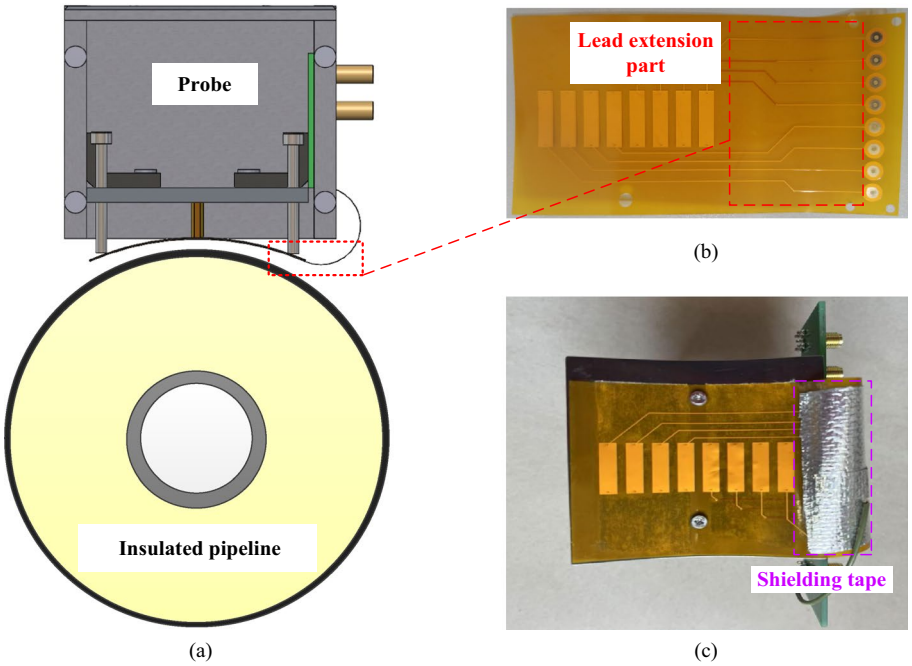


Fig. 17. Soft shielded tape applied to the extended trace sections of the substrate and grounded, completely eliminating the measurement error from parasitic capacitance introduced by these traces.

the optimal frequency band for suppressing 1/f noise and thereby improving the SNR. As shown in Fig. 18, the experimental results demonstrate that as the operating frequency of the capacitive bridge increased (from 3 to 10 kHz), the noise level of the capacitive signal decreased gradually, with the peak-to-peak noise amplitude reducing from 1×10^{-3} pF to 1.2×10^{-4} pF. These results confirm that the influence of 1/f noise was effectively suppressed to the 10^{-4} pF level.

It should be noted that increasing the bridge operating frequency indefinitely is not advantageous. First, once the capacitive measurement noise is reduced to the 10^{-4} pF level—approaching the display resolution limit of the current bridge setup—further noise reduction becomes practically meaningless. Moreover, setting the operating frequency too high can introduce parasitic capacitance coupling effects and exacerbate skin effects. Therefore, to balance noise suppression with minimizing the impact of parasitic parameters and skin effects on the measurement system, a comprehensive evaluation led to the selection of a final operating frequency range of 80–100 kHz for the capacitive bridge in this study.

On the other hand, capacitance measurement results are also influenced by parallel parasitic conductance (G_p). This parasitic conductance generates a leakage current ($I_{_leak}$), which compromises the accuracy of the capacitance measurements. The total measured current consists primarily of the true capacitive current ($I_{_c} = V / Z_{_c} = V\times(j\omega C)$) and $I_{_leak}$. At lower frequencies, $I_{_c}$ is relatively small, making $I_{_leak}$ non-negligible compared to $I_{_c}$ and resulting in significant current measurement error. Conversely, at higher frequencies, $I_{_c}$ becomes sufficiently large that $I_{_leak}$ is relatively negligible, leading to reduced current error and capacitance values closer to the true value. Therefore, the approach proposed earlier—appropriately increasing the operating frequency of the capacitive bridge and determining the optimal frequency band—not only suppresses 1/f noise but also reduces $I_{_leak}$, thereby minimizing current error and ensuring the accuracy of the capacitance measurements.

Determining the probing depth limit of the capacitive scanning sensor

To determine the probing depth limit of the capacitive scanning sensor developed in this study within the insulation layer of insulated pipelines, 12 mm diameter holes were drilled to various depths in the cross-section of the insulation layer. Titanium dioxide (TiO_2) cylindrical inserts were placed into these holes to simulate air–water voids. During the insertion and extraction of the TiO_2 cylindrical samples, changes in the capacitive scanning curve were monitored. A significant change in the curve indicates that the air–water void at the corresponding depth remains detectable. To make the changes in the test result curves more intuitive and obvious, we inserted and extract the TiO_2 samples twice respectively in each experiment, resulting in two distinct trends of change in the curves. The depths of the defect holes from the outer surface of the pipeline were set at three levels: 20 mm, 30 mm, and 50 mm, as shown in Fig. 19.

First, only the innermost single electrode pair in the sensor's array was activated to measure the air–water void at the shallowest depth of 20 mm. The results are shown in Fig. 20a. The variation in capacitance caused by inserting and extracting the TiO_2 sample was approximately $4\times10^{-}4$ pF. Compared to the noise amplitude of $1\times10^{-}4$ pF, the change in capacitance due to the presence or absence of the simulated void was significant. This indicates that the innermost single electrode pair can effectively detect the presence of an air–water void at a depth of 20 mm.

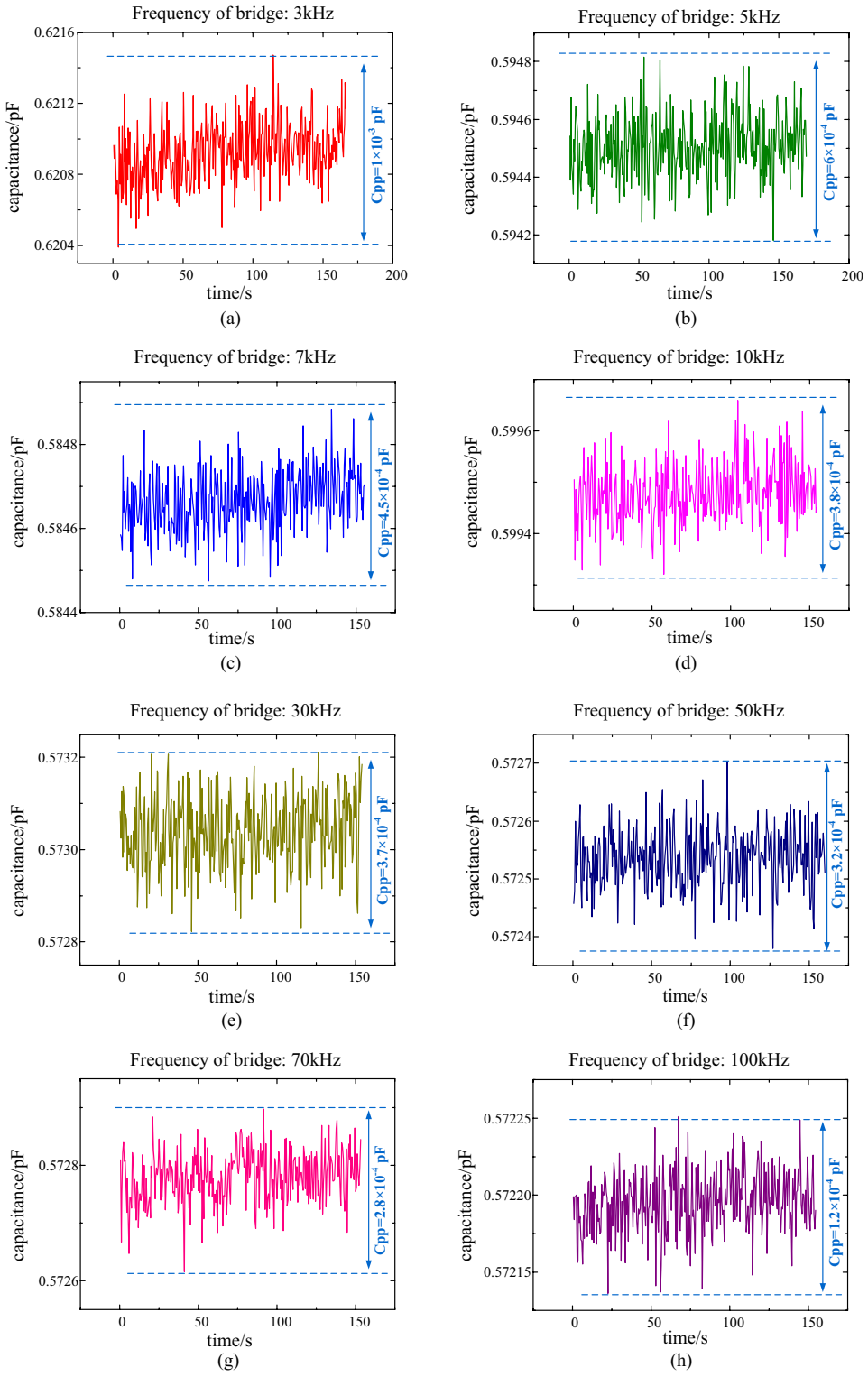


Fig. 18. By progressively increasing the operating frequency of the capacitive bridge, the optimal frequency band was identified to suppress 1/f noise. Subplots (**a**) to (**h**) correspond to bridge operation at 3 kHz, 5 kHz, 7 kHz, 10 kHz, 30 kHz, 50 kHz, 70 kHz, and 100 kHz, respectively.

Next, the same innermost single electrode pair was used to measure a void at a depth of 30 mm. The results, shown in Fig. 20b, revealed that the capacitance variation decreased to approximately $1.5 \times 10^{-}4$ pF, which is very close to the noise amplitude. This suggests that the innermost single electrode pair alone can not effectively detect defects at a depth of 30 mm.

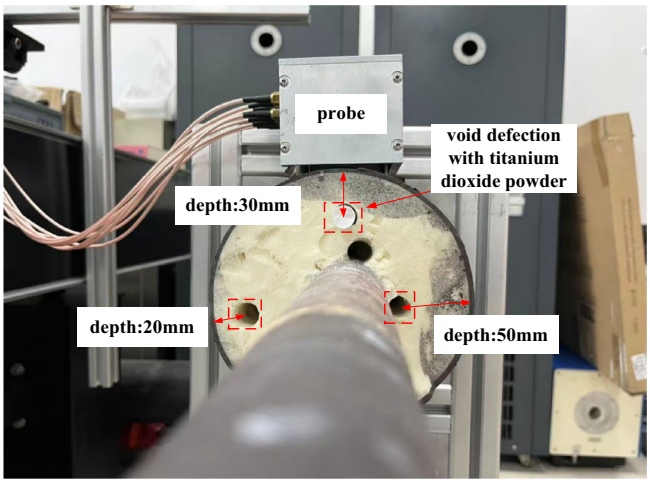


Fig. 19. Experimental setup for determining the probing depth limit of the capacitive scanning sensor.

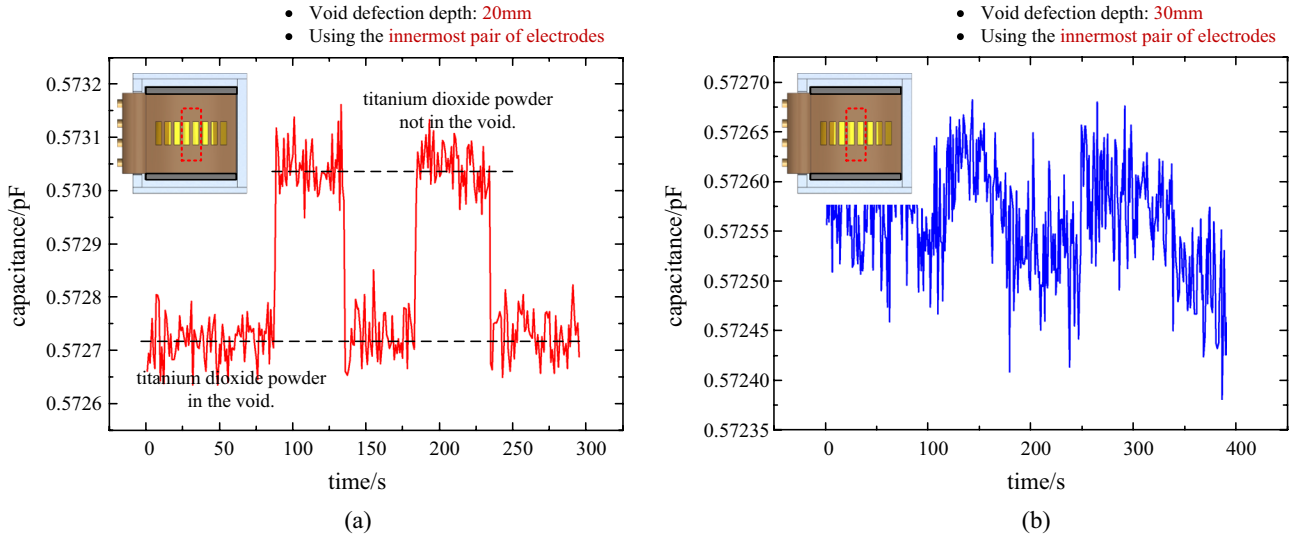


Fig. 20 . Measurement of air–water void defects at 20 mm and 30 mm depths using only the innermost single electrode pair in the sensor's capacitive array.

To extend the probing depth, the two innermost electrode pairs were activated to measure the void at 30 mm depth. The results are shown in Fig. 21a. The capacitance change during the insertion and extraction of the TiO_2 sample was about 1.8×10^{-4} pF, significantly higher than the noise level. This demonstrates that the two innermost electrode pairs can effectively detect the presence of an air–water void at 30 mm depth.

Subsequently, the same two innermost electrode pairs were used to measure a void at 50 mm depth. The results, shown in Fig. 21b, showed that the capacitance variation was very close to the noise amplitude, indicating that the two innermost electrode pairs are insufficient for effectively detecting defects at 50 mm depth.

Finally, to further extend the probing range to the bottom of the insulation layer at 50 mm depth, the three innermost electrode pairs and then all four electrode pairs in the array were activated separately to measure the void at 50 mm depth. The results are shown in Fig. 22a, b, respectively. The experimental results indicate that the three innermost electrode pairs still could not effectively detect the air–water void at 50 mm depth. Only by activating all four electrode pairs in the array could the presence of a defect at 50 mm depth be detected. Considering the diameter of the void itself, the depth of 50 mm represents the depth limit for the insulation layer thickness of the insulated pipeline used in this experiment.

Summary and conclusions

This work successfully developed and validated an integrated scanning system based on a curvature-adaptive flexible capacitive sensor for the early detection of defects in thermal insulated pipelines, a critical step in preventing corrosion under insulation (CUI).

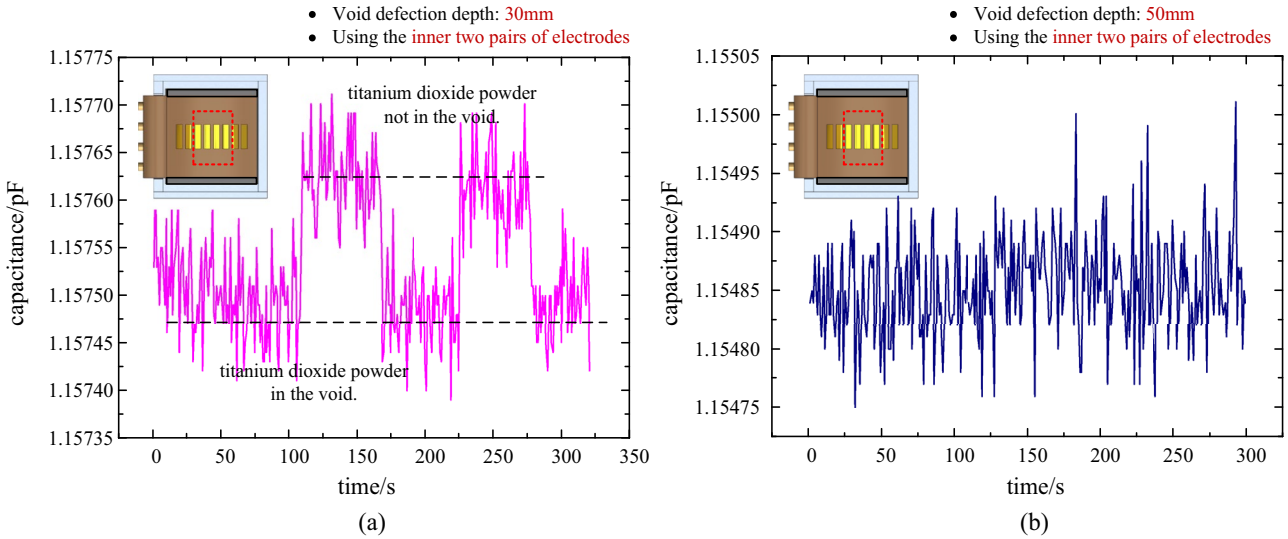


Fig. 21. Measurement of air–water void defects at 30 mm and 50 mm depths using the two innermost electrode pairs in the sensor's capacitive array.

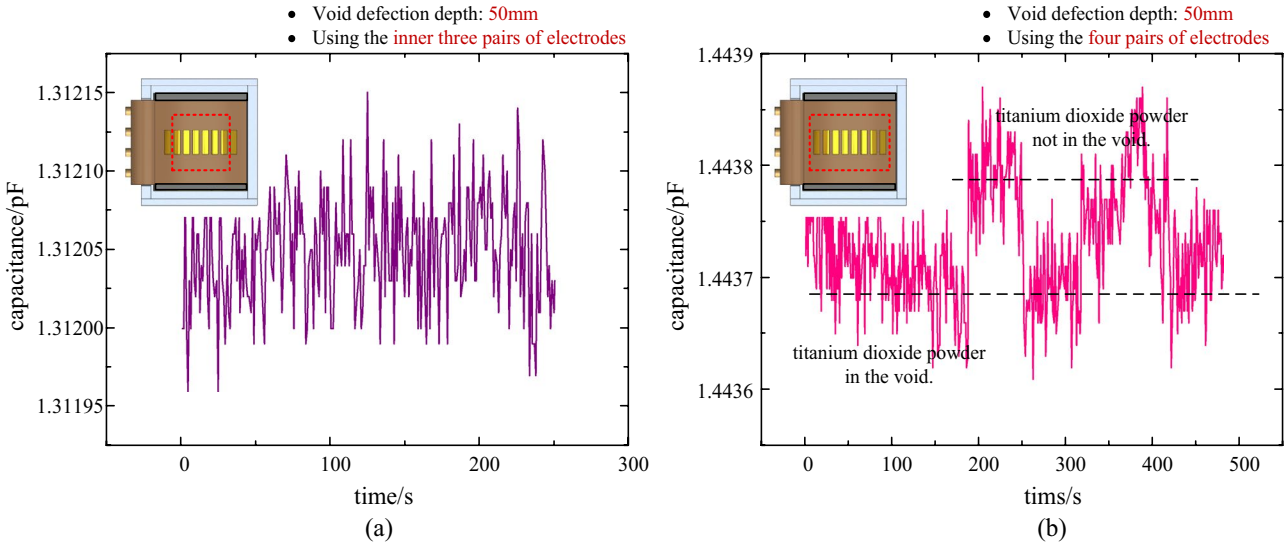


Fig. 22 . Measurement of the air–water void defect at 50 mm depth using the three innermost and all four electrode pairs in the sensor's capacitive array.

The core of the system is a novel flexible capacitive probe. Unlike conventional rigid probes, it incorporates an array of coplanar electrodes on a mechanically adjustable substrate, allowing it to conform to various pipeline curvatures. This design minimizes the air gap, enhancing electric field penetration into the insulation layer and improving detection sensitivity and signal-to-noise ratio. The electrode array generates a stratified electric field, and based on this characteristic, this study proposes a novel approach for estimating the depth of internal defects by identifying which electrode pair exhibits the maximum relative capacitance deviation—extending the system's capability beyond mere defect detection.

To address the practical challenge of signal aliasing between internal insulation defects and external jacket surface defects, by systematically increasing the lift-off height between the probe and the pipeline surface, we determined an optimal height that effectively suppresses the signal from surface topography while preserving the signal from internal defects, thereby achieving feature decoupling.

For scenarios with jacket defects, an automated recognition algorithm was implemented. An improved 1D-CNN model, incorporating multi-scale feature fusion and a channel attention mechanism, was trained to classify jacket surface conditions into four categories: normal, crack, corrosion, and sand/dust accumulation. The model demonstrated high accuracy and robust performance, with F1-scores exceeding 0.9 for all classes.

Comprehensive experiments were conducted to characterize the system. Key findings include:

The successful decoupling of internal void signals from jacket topography at an optimal lift-off height of ~ 1 mm.

Effective suppression scenarios of parasitic capacitance and 1/f noise, achieving a measurement sensitivity of 10^{-4} pF by operating the capacitance bridge in the 80–100 kHz frequency range.

Validation of the depth-sensing capability, confirming that activating more electrode pairs in the array extends the probing depth, successfully detecting simulated defects at the maximum tested depth of 50 mm.

In summary, this research provides a comprehensive and practical solution that moves beyond simply detecting CUI to enabling early warning by identifying its precursors. The synergy of the flexible hardware design, depth-sensing methodology, feature decoupling strategy, and intelligent classification algorithm establishes a new paradigm for non-invasive, in-situ pipeline integrity monitoring.

Data availability

Data underlying the results presented in this paper are not publicly available at this time but may be obtained from the authors upon reasonable request.

Received: 7 February 2026; Accepted: 31 March 2026
Published online: 14 April 2026

References

1. Eltai, E. O., Scantlebury, J. D. & Koroleva, E. V. Protective properties of intact unpigmented epoxy coated mild steel under cathodic protection. *Prog. Org. Coat.* **73**, 8–13. https://doi.org/10.1016/j.porgcoat.2011.09.009 (2012).
2. Delahunt, J. Corrosion under thermal insulation and fireproofing - an overview. In *Proceedings of the NACE Annual Conference & Exposition* (Carmagen Engineering, Inc., Rockaway, NJ, 2003).
3. Shim, H. S., Choi, M. S., Lee, D. H. & Hur, D. H. A prediction method for the general corrosion behavior of alloy 690 steam generator tube using eddy current testing. *Nucl. Eng. Des.* **297**, 26–31. https://doi.org/10.1016/j.nucengdes.2015.11.025 (2016).
4. Rakvin, M., Markucic, D. & Hizman, B. Evaluation of pipe wall thickness based on contrast measurement using computed radiography (CR). *Procedia Eng.* **69**, 1216–1224. https://doi.org/10.1016/j.proeng.2014.03.154 (2014).
5. Twomey, M. Inspection techniques for detecting corrosion under insulation. *Mater. Eval.* **55**, 129–132. https://doi.org/10.1361/105293197774376981 (1997).
6. Winnik, S. *Corrosion-Under-Insulation (CUI) Guidelines* 2nd edn. (Woodhead Publishing, 2016).
7. Robin, E. Use of Microwaves for the Detection of Corrosion Under Insulation. PhD thesis, Imperial College London (2012).
8. Yin, X., Hutchins, D., Chen, G. & Li, W. Detecting surface features on conducting specimens through an insulation layer using a capacitive imaging technique. *NDT. E. Int.* **52**, 157–166. https://doi.org/10.1016/j.ndteint.2012.08.004 (2012).
9. Yin, X. & Hutchins, D. Non-destructive evaluation of composite materials using a capacitive imaging technique. *Compos. Part B Eng.* **43**, 1282–1292. https://doi.org/10.1016/j.compositesb.2011.10.018 (2012).
10. Yin, X., Hutchins, D. & Chen, G. Preliminary studies on the design principles of capacitive imaging probes for non-destructive evaluation. *Int. J. Appl. Electromagn. Mech.* **42**, 447–470. https://doi.org/10.3233/JAE-131676 (2013).
11. Yin, X., Hutchins, D., Chen, G. & Li, W. Investigations into the measurement sensitivity distribution of coplanar capacitive imaging probes. *NDT. E. Int.* **58**, 1–9. https://doi.org/10.1016/j.ndteint.2013.04.001 (2013).
12. Amato, S., Hutchins, D., Yin, X., Ricci, M. & Laureti, S. Capacitive imaging using fused amplitude and phase information for improved defect detection. *NDT. E. Int.* **124**, 102547. https://doi.org/10.1016/j.ndteint.2021.102547 (2021).
13. Yin, X., Hutchins, D., Diamond, G. & Purnell, P. Non-destructive evaluation of concrete using a capacitive imaging technique: preliminary modelling and experiments. *Cem. Concr. Res.* **40**, 1734–1743. https://doi.org/10.1016/j.cemconres.2010.08.015 (2010).
14. Zeng, T. et al. Combined sensor with spatial gradient profile for capacitive imaging. *IEEE Sens. J.* **23**, 8826–8838. https://doi.org/10.1109/JSEN.2023.3251278 (2023).
15. Abdollahi-Mamoudan, F., Ibarra-Castanedo, C. & Maldague, X. P. V. Non-destructive testing and evaluation of hybrid and advanced structures: a comprehensive review of methods, applications, and emerging trends. *Sensors* **25**, 3635. https://doi.org/10.3390/s25123635 (2025).
16. Abdollahi-Mamoudan, F., Ibarra-Castanedo, C. & Maldague, X. P. V. Advancements in and research on coplanar capacitive sensing techniques for non-destructive testing and evaluation: a state-of-the-art review. *Sensors* **24**, 4984. https://doi.org/10.3390/s24154984 (2024).
17. Abdollahi-Mamoudan, F., Savard, S., Ibarra-Castanedo, C., Filleter, T. & Maldague, X.P.V. Coplanar capacitive sensing as a new electromagnetic technique for non-destructive evaluation. In *Proceedings of the 48th Annual Review of Progress in Quantitative Nondestructive Evaluation (QNDE 2021)* (ed. American Society of Mechanical Engineers) V001T05A002 (American Society of Mechanical Engineers, 2021). https://doi.org/10.1115/QNDE2021-74739
18. Abdollahi-Mamoudan, F., Ibarra-Castanedo, C., Filleter, T. & Maldague, X. P. V. Experimental study and FEM simulations for detection of rebars in concrete slabs by coplanar capacitive sensing technique. *Sensors* **22**, 5400. https://doi.org/10.3390/s22145400 (2022).
19. Abdollahi-Mamoudan, F., Savard, S., Filleter, T., Ibarra-Castanedo, C. & Maldague, X. P. V. Numerical simulation and experimental study of capacitive imaging technique as a nondestructive testing method. *Appl. Sci.* **11**, 3804. https://doi.org/10.3390/app11093804 (2021).
20. Abdollahi-Mamoudan, F., Savard, S., Ibarra-Castanedo, C., Filleter, T. & Maldague, X. P. V. Influence of different design parameters on a coplanar capacitive sensor performance. *NDT & E Int.* **126**, 102588. https://doi.org/10.1016/j.ndteint.2021.102588 (2022).
21. Abdollahi-Mamoudan, F., Savard, S., Ibarra-Castanedo, C., Filleter, T. & Maldague, X. P. V. Multi-electrode coplanar capacitive probe with various arrangements for non-destructive testing of materials. *IEEE Sens. J.* **22**, 8134–8146. https://doi.org/10.1109/JSEN.2022.3155974 (2022).

Author contributions

Tao Zeng and Songzhe Chai were responsible for the design, material preparation, structural construction, data collection, experimental verification and other related work of this paper. Jinxin Xu undertook the proofreading of the manuscript, and Su'an Xu was in charge of the guarantee of the laboratory site and other supporting work.

Funding

This work was supported by the National Natural Science Foundation of China (Grant Nos. 62573395, 52005472, 62373339, 52375555), Natural Science Foundation of Zhejiang Province (Grant No. LQ20E050015,

LZ24F030007), Fundamental Research Funds for the Provincial Universities of Zhejiang (Grant No. 2023YW12).

Declarations

Competing interests
The authors declare no competing interests.

Additional information
Correspondence and requests for materials should be addressed to T.Z.

Reprints and permissions information is available at www.nature.com/reprints.

Publisher's note Springer Nature remains neutral with regard to jurisdictional claims in published maps and institutional affiliations.

Open Access This article is licensed under a Creative Commons Attribution-NonCommercial-NoDerivatives 4.0 International License, which permits any non-commercial use, sharing, distribution and reproduction in any medium or format, as long as you give appropriate credit to the original author(s) and the source, provide a link to the Creative Commons licence, and indicate if you modified the licensed material. You do not have permission under this licence to share adapted material derived from this article or parts of it. The images or other third party material in this article are included in the article's Creative Commons licence, unless indicated otherwise in a credit line to the material. If material is not included in the article's Creative Commons licence and your intended use is not permitted by statutory regulation or exceeds the permitted use, you will need to obtain permission directly from the copyright holder. To view a copy of this licence, visit http://creativecommons.org/licenses/by-nc-nd/4.0/.

© The Author(s) 2026